

V

Journal of Hydrology
Manuscript Draft

Manuscript Number: HYDROL21937

Title: Accurate determination of permeability of fractured rocks using micro-computed tomography images

Article Type: Research Paper

Keywords: fractured media, micro-CT imaging, fracture aperture, permeability

Abstract: A novel method for accurate determination of permeability in fractured media is introduced. The method employs high-resolution scanning electron microscope (SEM) data for calibration of micro-computed tomography (micro-CT) images. Micro-CT is used to obtain 3D images of a highly fractured sample with a resolution of 16.5 μ m and SEM is applied to obtain images with nanometer resolution from thin sections of the sample. The SEM images are registered to the micro-CT images to facilitate image segmentation and generation of a calibration curve. The calibration curve correlates the gray-scale values at the mid-point of each fracture to the true apertures measured from SEM data. Thinned fractures of two subset are extracted and used to extract the gray-scale values at the mid-point of fractures. These are then converted to the true apertures values using the calibration curve and subsequently grown by the adjustment algorithm to produce 3D calibrated binary images. The connectivity and aperture size distribution of the subsets before and after calibration are quantified. The results indicate that a large amount of valuable information is preserved when the calibration technique is used. The permeability of the subsets after and before calibration is computed using a direct numerical simulator and compared with the experimental permeability. The computed permeabilities demonstrate that using the non-calibrated images generates massive errors in permeability while the calibrated images produce more realistic permeability that coincides with the experimental result. The method can be applied to fractured rocks for better prediction of permeability and other petrophysical properties.



Accurate determination of permeability of fractured rocks using micro-computed tomography images

Hamed Lamei Ramandi*, Peyman Mostaghimi, Ryan T. Armstrong

School of Petroleum Engineering, The University of New South Wales, Sydney NSW 2052, Australia

*Corresponding author address: School of Petroleum Engineering, The University of New South Wales, Sydney NSW 2052, Australia. E-mail addresses: h.lameiramandi@unsw.edu.au (H. Lamei Ramandi), p.mostaghimi@unsw.edu.au (P. Mostaghimi), ryan.armstrong@unsw.edu.au (R. T. Armstrong),

Abstract

A novel method for accurate determination of permeability in fractured media is introduced. The method employs high-resolution scanning electron microscope (SEM) data for calibration of micro-computed tomography (micro-CT) images. Micro-CT is used to obtain 3D images of a highly fractured sample with a resolution of $16.5\mu\text{m}$ and SEM is applied to obtain images with nanometer resolution from thin sections of the sample. The SEM images are registered to the micro-CT images to facilitate image segmentation and generation of a calibration curve. The calibration curve correlates the gray-scale values at the mid-point of each fracture to the true apertures measured from SEM data. Thinned fractures of two subset are extracted and used to extract the gray-scale values at the mid-point of fractures. These are then converted to the true apertures values using the calibration curve and subsequently grown by the adjustment algorithm to produce 3D calibrated binary images. The connectivity and aperture size distribution of the subsets before and after calibration are quantified. The results indicate that a large amount of valuable information is preserved when the calibration technique is used. The permeability of the subsets after and before calibration is computed using a direct numerical simulator and compared with the experimental permeability. The computed permeabilities demonstrate that using the non-calibrated images generates massive errors in permeability while the calibrated images produce more realistic permeability that coincides with the experimental result. The method can be applied to fractured rocks for better prediction of permeability and other petrophysical properties.

Keywords: fractured media, micro-CT imaging, fracture aperture, permeability

1. Introduction

Permeability is a fundamental parameter that governs fluid transport in geologic media. Its magnitude and spatial distribution plays an important role in all studies covering underground fluid migration and have been studied by a number of researchers (Gangi, 1978; Illman, 2006; Jazayeri Noushabadi et al., 2011; Latham et al., 2013; Scheidegger, 1963; Wang and Park, 2002). Fractured rock masses generally contain intact rock materials and fractures, with the latter

acting as the principal conduit of fluid flow. One of the most complex fractured porous media is coal where a natural system of fracture exists containing two sets of orthogonal fractures, i.e. face and butt cleats, which are also orthogonal to the bedding (Laubach and Tremain, 1991; Laubach et al., 1998; Ting, 1977). This natural fracture network provides a high permeability conduit that is responsible for most of the permeability in the media while micro-pores have a limited impact on the permeability (Clarkson and Marc Bustin, 1996; Moore, 2012; Puri et al., 1991). The mechanical opening of this natural fracture network is one of the key factor in coal permeability that has been measured by many researchers (Close and Mavor, 1991; Gamson et al., 1993; Mazumder et al., 2006; Su et al., 2001; Yao et al., 2009).

A variety of destructive (Brown et al., 1986; Gentier et al., 1989; Pyrack-Nolte et al., 1987) and nondestructive (Detwiler et al., 1999; Huo et al., 2016; Keller, 1998; Ketcham et al., 2010; Kumar et al., 1997; Mazumder et al., 2006; Renshaw et al., 2000; Robert et al., 1993; Van Geet and Swennen, 2001; Vandersteen et al., 2003; Verhelst et al., 1995; Yao et al., 2009) methods have been used for measuring fracture aperture sizes in rocks. Using a nondestructive method for characterization of a fractured rock is more advantageous since obtaining a fractured sample in which a permeable fracture network is preserved is challenging (Ortega et al., 2006). When such a sample is obtained, prior to sample breakage, numerous experiments are required to be performed on the sample for petrophysical characterization. In the proposed nondestructive methods, X-ray micro-computed tomography (micro-CT) holds the advantage that it can be used for flow simulation (Armstrong et al., 2014a; Armstrong et al., 2014b; Berg et al., 2014; Huo et al., 2016).

A common problem with micro-CT deals with the balance between obtaining a large enough representative image of the sample and the image resolution that needs to resolve its structure. While scanning larger samples, the image resolution in the direction normal to a fracture, is often not enough, i.e. represented by only a few voxels (Ketcham et al., 2010). Micrometer-sized fracture aperture sizes typically occur near the resolution limit of micro-CT instruments. This makes fracture network visualization and aperture size measurement problematic. In an air-filled (dry) micro-CT image, low attenuation coefficients (gray-scale values) are observed where a fracture exists. This is due to the density deficit of the fracture. However, attenuation coefficients are also reduced in the vicinity of a fracture. This is due to smearing of the X-ray attenuation and so-called partial volume effects (Ketcham, 2005; Ketcham and Carlson, 2001; Weerakone and Wong, 2010). The partial volume effect causes the gray-scale values to reduce in the voxels adjacent to the fracture. This is because the voxel volume contains a number of different materials, in this case fracture and matrix, that results in a gray-scale value that characterizes some average of the properties (Ketcham and Carlson, 2001). Moreover, when material properties change spatially over small distances, smearing of X-ray attenuation occurs due to the finite beam width and oversampling associated with the micro-CT

instrument (Johns et al., 1993; Ketcham, 2005). As a result, smearing of the X-ray attenuation and partial volume effects cause the gray-scale transition between neighboring objects with different densities to span several voxels rather than being sharp (Ketcham, 2005). This can result in mislabeling of fractures during the segmentation process and consequently gross overestimation/underestimation of aperture widths and thus fractured rock permeability.

A few alternative techniques have been proposed for measuring fracture aperture sizes using micro-CT data. These methods use the local gradient in voxel values from the raw and/or filtered images. These include peak height (PH) (Mazumder et al., 2006; Vandersteen et al., 2003; Verhelst et al., 1995), full-width-half-maximum (FWHM) (Peyton et al., 1992), and missing attenuation (MA) (Johns et al., 1993; Mazumder et al., 2006; Vandersteen et al., 2003). PH carries the advantage that it is independent of fracture direction (Vandersteen et al., 2003) and can estimate relatively small aperture sizes (Mazumder et al., 2006). These approaches can be used either by creating a calibration curve (Mazumder et al., 2006) or using a calibration-free method (Huo et al., 2016). In the previous studies, the relationship between the FWHM, MA or PH and fracture aperture sizes is determined using careful calibration with spacers of known thickness, which allows for the generation of a calibration curve (Johns et al., 1993; Ketcham et al., 2010; Mazumder et al., 2006; Vandersteen et al., 2003). One major drawback of these approaches is that they require at least two sets of micro-CT images; one for imaging fractures of known dimensions and another for the sample of interest. However, using this type of calibration curve for measuring the aperture sizes in the image of interest is not exact. This is because the attenuation coefficient of each material can vary with any change in the imaging conditions and to compensate for this images must be rescaled, which results in uncertainties. This suggests that each generated calibration curve is matchless and cannot be used for the images that are obtained at different imaging conditions. However, recently we (Ramandi et al., 2016a) introduced a new technique in which SEM images that are registered to micro-CT data are used to generate the calibration curve. In this way, the need for acquiring two sets of micro-CT images and its problematic consequences of rescaling are eliminated. Nevertheless, a comprehensive method for using the calculated aperture sizes to estimate permeability on a full 3D micro-CT image is lacking in the literature.

Herein, we develop a framework in which we acquire a 3D image of a fractured rock sample at the core-scale and implement a workflow to reconstruct the image with accurate fracture aperture sizes and thus provide realistic permeability measurements from direct numerical simulation. We first segment the fractures and then thin the fractures to a single voxel at the mid-point of the fracture aperture. This thinned fracture is then used to extract the gray-scale values at the mid-point of each fracture in the original micro-CT image. The extracted values are converted to the aperture sizes using an SEM generated calibration curve. At this point, voxel values along the thinned fracture correspond to true aperture sizes. Then an adjustment

algorithm proceeds to open the calibrated-thinned fracture according to the aperture values to create a binary image. Herein, we validate the workflow by comparing fracture aperture size distributions from SEM and the result from the calibration technique and also compare simulated permeabilities to experimentally measured permeability.

2. Methodology

2.1. Data collection methods

For micro-CT imaging, a high-resolution helical scanner is used in this study. The instrument is a part of the micro-computed tomography facility at the Australian National University ([Sheppard et al., 2014](#)). The scanner settings are provided in the Table 1. The collected projections from the instrument are reconstructed to produce a 3D representation of the sample (tomograms). Each data point in the tomogram characterizes the effective X-ray attenuation coefficient. This is displayed in 16-bit gray-scale images.

[Table 1. The scanning parameters of the instrument used in this study.](#)

Scanning parameters	Specifications
Acquisition time	23 hrs
Energy of X-ray	120 kV (100 mA)
Scanning operation	Helical system
X-ray beam form	Cone beam
Total number of projections	10106
Pitch	25.938 mm
The angular step	0.002493 Rad
The vertical step	0.010293 mm
Beam hardening filter	3 mm aluminum

The selected sample for imaging is a coal sample that has a diameter of 25 mm and a length of 37 mm. The geology of the region and sample specifications are discussed in detail in ([Ramandi et al., 2016b](#)). The sample is initially scanned in as-received condition, i.e. dry air-filled fractures (Figure 1a). For highlighting all fluid-accessible pores and fractures the sample is saturated with an X-ray attenuating fluid and re-imaged, i.e. wet image with fluid-filled fractures (Figure 1b). The X-ray attenuating fluid is a mixture of 1.5 molar Sodium Iodide (NaI) and 1.0 molar Potassium Chloride (KCl). The saturation process involves saturating the sample under vacuum, and injecting the fluid at a high pressure of ~ 670 . In this way, all the fluid-accessible pores and fractures are saturated. Images, wet and dry, have a resolution of 16.5 μm . A cubic subset of

UNITS?

5.62 mm^3 (M1) and a rectangular prismatic subset of $3.3 \times 3.3 \times 2 \text{ mm}$ (M2) are obtained from cylindrical image of the sample. These subsets contain well-developed fracture networks with a range of fracture apertures above and below the image resolution. After micro-CT imaging the sample is cut and polished for SEM imaging. Secondary Electron and Backscatter Electron SEM techniques are accomplished using a Hitachi S3400 at the Electron Microscope Unit of the Mark Wainwright Analytical Centre at the University of New South Wales.

The dry and wet images are then registered using the technique developed by [Latham et al. \(2008\)](#). The method performs a voxel-to-voxel registration of the dry and wet images. The technique brings the dry and wet images into geometric alignment and generates a pair of images with identical dimensions allowing for a voxel-to-voxel comparison of the images. After image registration, dry and wet image subtraction provides the difference image (Figure 1c). The difference image locates the fractured regions. Also, it quantifies effective micro-porosity of individual voxels that are not readily recognizable with conventional imaging techniques ([Ramandi et al., 2015](#)). This allows for the visualization of a more representative fracture network than with conventional imaging of the dry sample.

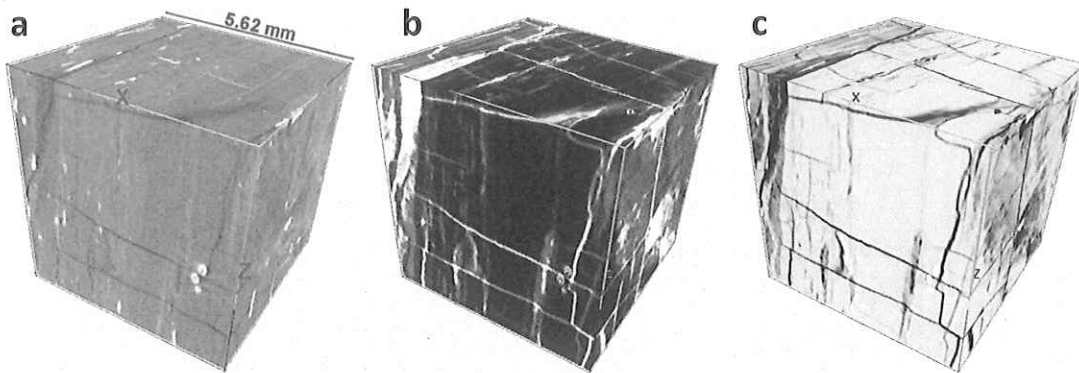


Figure 1. a: a registered 5.6 mm cube of dry micro-CT image (black= pores and fractures, gray= macerals and white = minerals), b: the same cube after saturation with X-ray attenuating fluid (white = minerals and saturated pores and fractures, and black = macerals), c: the difference image of the same cube (inverted difference image, black= pores and fractures, gray= macerals and white = minerals).

2D-to-3D registration technique developed by [Latham et al. \(2008\)](#) is used to register SEM images to micro-CT images. The algorithm searches the entire block of the tomogram to find the exact slice that matches the SEM image. Then the algorithm performs all the required translation, rotation, warping and scaling transformations to coincide each point in the SEM to the corresponding slice from the 3D tomogram. This allows for a direct comparison of the higher-resolution information provided in the SEM data to that in the micro-CT data, which assists in selection of appropriate threshold levels and generation of a calibration curve.

2.2. Image processing methods

The micro-CT images contain attenuation coefficients that are displayed in a gray-scale multiphase image. Image segmentation involves converting the gray-scale multiphase image into unique well-defined regions (phases) that are homogeneous with respect to some characteristic (Sheppard et al., 2004). A bimodal intensity histogram for the sample that represents voids, intact matrix as individual peaks is ideal for image segmentation. However, there are often features at or below the instrument resolutions which blur the sharp edges at phase boundaries (Ketcham, 2005; Sheppard et al., 2004). These blurred features spread out the intensity histogram and make the visualization and segmentation difficult for complex multi-mineral and fractured samples. To remove noise and sharpen the images a nonlinear anisotropic diffusion filter followed by the unsharp mask is applied (Sakellariou et al., 2007; Sheppard et al., 2004). These are shown to be highly effective at sharpening edges without excessively intensifying the noise (Sheppard et al., 2004). Converging active contours (CAC) that is developed based on a combination of the watershed method (Vincent and Soille, 1991) and active contour methods (Caselles et al., 1997) is used to yield satisfactory segmentation results. CAC uses intensity gradient and intensity information simultaneously (Schlüter et al., 2014; Sheppard et al., 2004) and it has been successfully applied to cubic datasets of up to 2000^3 voxels (Arns et al., 2005; Jones et al., 2007; Ramandi et al., 2015; Ramandi et al., 2016b; Saadatfar et al.; Sheppard et al., 2004; Sok et al., 2010). The algorithm proceeds by inputting two thresholds that are chosen through a detailed inspection of the gray-scale histogram image. The algorithm tags the voxels with gray-values below the lower threshold as void and voxels with gray-scale values greater than the upper threshold as solid. The values between the lower and upper thresholds are tagged as unallocated. The algorithm simultaneously expands the tagged regions towards each other, within the unallocated region, to place the boundary at the points where two contours join (Schlüter et al., 2014; Sheppard et al., 2004). The local gradient and the distance of the local voxel value to the mean voxel value of its matching phase determine the speed at which the boundaries expand (Schlüter et al., 2014). We preformed three successive CACs on the difference image to segment it into four phases: (1) resolved void that includes fractures and pores that exists at or above the micro-CT resolution limit, (2) sub-resolution fractures and pores that exist below the micro-CT resolution limit, (3) coal macerals that includes organic regions of the coal that are not penetrated by X-ray attenuating fluid, and (4) mineral phases (inorganic) that included high density regions in the coal (Figure 2b).

After CAC, two basic operations of mathematical morphology, dilation and erosion (Serra, 1986) is used to separate the sub-resolution pores from sub-resolution fractures. The erosion filter shrinks image features and eliminates features with a radius less than the kernel while dilation filters expand features in the image and close any gaps (Quackenbush, 2004). Erosion followed by dilation (opening) removes small or narrow elements without effecting large ones (Dong,

1997). Buie et al. (2007) applied morphological closing operations (dilation followed by erosion) on a micro-CT image of bone to remove the small channels in bone. We erode the sub-resolution pores and fracture phase to remove the sub-resolution fractures. Then the eroded region is dilated to obtain its initial shape without the sub-resolution fractures. This is masked on the original image to obtain the intersection regions between the original image and eroded-dilated image. This separates the sub-resolution pores, i.e. intersection region, and sub-resolution fractures, i.e. the remaining regions (Figure 2c). To avoid loss of detail due to dilation and erosion operations, the kernel radius for this filter is made as small as possible while not removing the microporosity regions. Note that this step is only to identify fractures from microporosity in subsequent steps we re-calibrate the apertures sizes and thus any manipulation of fracture geometries by the opening algorithm is accounted for in the later steps.

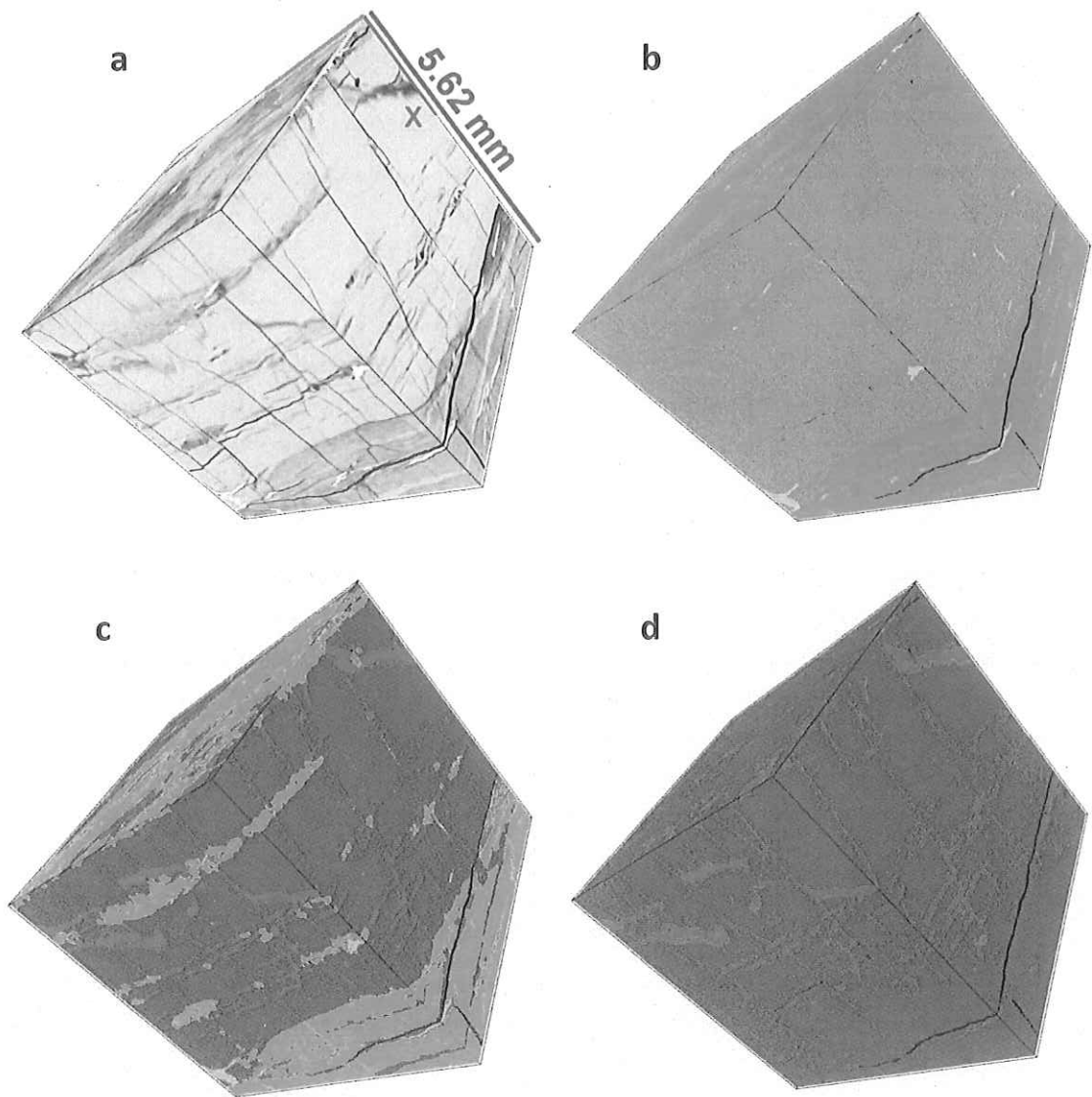


Figure 2. 3D visualization of sample M1. a: the difference image (dark = fractures and pores, gray = macerals and white= minerals), b: the conventional segmented image (black = resolved fractures and pores, green = sub-resolution fractures and pores, gray = macerals, and orange = minerals), c: segmented image using mathematical morphology (black = resolved fractures and pores, green = sub-resolution micro-porous region, red = sub-resolution fractures, gray = macerals, and orange = minerals) , d: the fracture network of the sample (red = the fracture network, gray, macerals).

2.3. Image calibration methods

To measure the aperture size at each fracture point, the Eq. 1 derived from the calibration curve presented in Figure 4 of [Ramandi et al. \(2016a\)](#) is used. The calibration curve is generated based on the true apertures obtained from the high-resolution SEM images, methods discussed

in [Ketcham et al. \(2010\)](#), and the fracture mid-point gray-scale value obtained from micro-CT image. For details on the generation of the calibration curve refer to our previous works ([Mostaghimi et al., 2015](#); [Ramandi et al., 2016a](#)).

$$A = 0.0717 gs - 4544$$

Eq. 1

where A is the aperture in μm and gs is the gray-scale value. We use an upsampling method based on the Catmull-Rom interpolation ([Catmull and Rom, 1974](#)) to obtain a calibrated image with a higher voxel resolution than the original image. In this technique, the number of voxels are increased by a factor of ϵ , which is chosen by the user, to generate an image with a smaller voxel size ([Cantrell and Michaels, 2010](#); [James, 2012](#); [Leone et al., 2009](#)). This allows for assigning aperture sizes smaller than the image resolution to the fracture ([Ramandi et al., 2016a](#)). To extract the gray-values at the mid-point of each fracture, each non-calibrated segmented image is upsampled and thinned to a single voxel width. Since the existing 3D thinning algorithms ([Lee et al., 1994](#); [Lindquist et al., 1996](#); [Lindquist and Venkatarangan, 1999](#); [Pudney, 1998](#)) are optimized for tubular and porous structures, e.g. bones, vessels, rock pores, they do not provide a proper thinning for fractures with planar structures. This point will be demonstrated in the results and discussion section. Alternatively, we use a stack of 2D skeletons in the direction of flow to generate a thinned fracture. The constructed thinned fracture is then used to obtain coordinates of each fracture aperture mid-point. The coordinates are then used to acquire the gray-scale value at the mid-point of each fracture aperture from the upsampled dry micro-CT image. Subsequently, the calibration curve is applied to derive the true aperture sizes from the acquired gray-scale values. This generates a weighted thinned fracture along which the weighting values correspond to the true aperture size. Lastly, the aperture adjustment algorithm marches along the thinned fracture and opens it according to the corresponding aperture values. This creates a new binary image in which the fracture network is obtained from the micro-CT images while the aperture sizes are assigned based on the calibration curve obtained from the high-resolution SEM data ([Ramandi et al., 2016a](#)).

2.4. Connectivity and permeability measurement methods

Both the connectivity index and permeability measurements are used to quantify the resulting fracture networks and validate the presented method. The segmented image is used to tag the fracture network that percolates from inlet to outlet, using a voxel neighborhood connectivity requirement of 6 ([Knackstedt et al., 2007](#)). The percolating network is then used to measure the

connectivity index. The connectivity index is a fundamental topologic measure that is derived from Euler number. It is defined as the maximum number of branches that can be broken within the network before splitting the network in two parts (Odgaard and Gundersen, 1993).

$$\beta_1 = 1 - \Delta\chi$$

Equation 2

where β_1 is the connectivity index and $\Delta\chi$ is the Euler characteristic of the sample. Since the connectivity depends on the sample size, the connectivity density (CD) is used to show the degree of the connectivity (Odgaard and Gundersen, 1993). CD is a measure of the degree of connectivity of percolating network normalized by total volume (V).

$$CD = \frac{\beta_1}{V}$$

Equation 3

After identifying the percolating cluster, flow can be simulated in the fractured medium using computational fluid dynamics methods to obtain pressure and velocity fields (Mostaghimi and Mahani, 2010; Mostaghimi et al., 2014). Permeability prediction is obtained based on the finite volume solution of the Stokes equation

$$\mu \nabla^2 \bar{u} = \nabla P$$

Equation 4

where \bar{u} is the velocity vector, P is pressure, and μ is the fluid viscosity. A no-slip boundary condition is applied on the solid surfaces. The experimental permeability is calculated with an unsteady state Automated Permeameter which is designed based on the work presented by Jonès (1972). The instrument is able to measure sample permeabilities ranging from 0.001 to 10000 mD.

3. Result and discussion

Fracture geometry and topology has a direct impact on the permeability of fractured rocks; therefore, it is critical to capture these parameters accurately for prediction of flow properties from 3D images of fractured rocks. A particular problem associated with the partitioning of fractures from micro-porous sub-resolution regions is that the gray-scale voxel values of both regions are very similar. This makes segmentation of the fractures challenging. In many cases fractures with aperture sizes near the resolution limit can connect the larger dominant

fractures and thus significantly change the topology of the fracture system. In Figure 2c, we demonstrate the ability of the mathematical morphological operations in separating the sub-resolution features and fractures. This provides a 3D binary image in which the entire fracture network is available, i.e. we capture both the dominant fractures and those with aperture sizes near the resolution limit. This complete fracture network is then used as the input data for the presented 3D calibration technique.

Along with capturing the entire fracture network, precise aperture measurement and assignment are the determining factors for measuring an accurate permeability. Figure 3 shows an SEM image of a fracture in the sample that is registered to the corresponding micro-CT slice. The thinning of the fracture is extracted using the non-calibrated segmented image. Then, the gray-values along the thinned fracture are extracted and converted to the true apertures using the calibration curve. Comparison of the apertures measured from the SEM image (Figure 3a) and the non-calibrated image (Figure 3c) shows the significant error that occurs by mislabeling of voxels in the fractured region. This can have a huge impact on the permeability. While comparison of the same region measured from the SEM image and calculated aperture values (Figure 3e) demonstrate that the error in measuring aperture is considerably reduced. This suggests that more satisfactory results can be achieved when such a calibration technique is used.

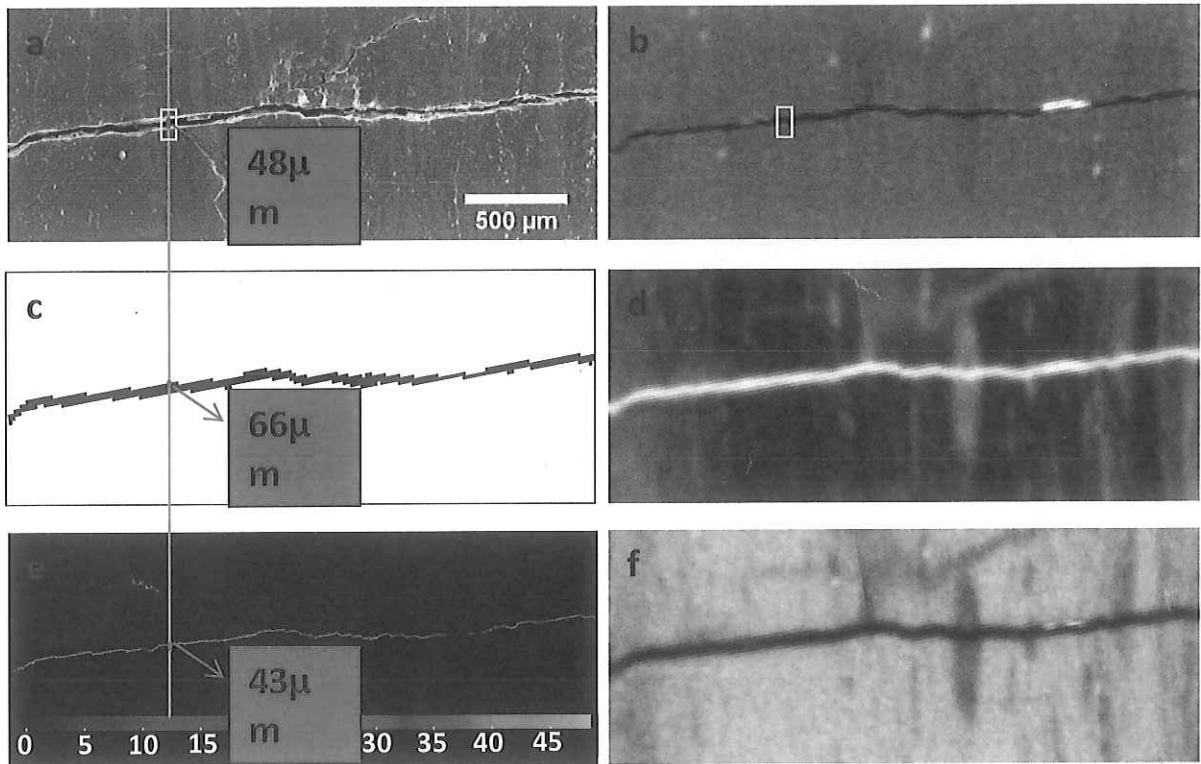


Figure 3. a: the registered SEM image ($2.34 \mu\text{m}/\text{pixel}$), b: the registered dry micro-CT image ($(16.5 \mu\text{m} \text{ voxels})$ black= pores and fractures, gray= macerals and white = minerals), c: segmented fracture from the same slice using non-calibrated segmentation method ($16.5 \mu\text{m} \text{ voxels}$), d: the registered wet micro-CT image ($(16.5 \mu\text{m} \text{ voxels})$ white = minerals and saturated pores and fractures, and black = macerals), e: the weighted thinned fracture of the same slice, f: the difference image of the same slice ($(16.5 \mu\text{m} \text{ voxels})$ inverted difference image, black= pores and fractures, gray= macerals and white = minerals).

The next step is to determine the best approach for extracting the mid-point aperture voxels from the segmented micro-CT image. Figure 4a shows the segmented fractures while Figure 4b and c demonstrate different methods to extract the mid-point aperture voxel. Figure 4b displays the results using a 3D medial axis extraction algorithm, as described by Lee et al. (1994); Lindquist et al. (1996); (1999); Pudney (1998). The results demonstrate that the 3D generation of the medial axis for the fractured sample with planner structures fails to provide an acceptable result. This is because the methods are optimized to provide a medial axis for tubular or porous structures whereas fractures are long and planner. An alternative method is to restrict the thinned fracture construction to a 2D plan and repeat this for the entire image, i.e. restrict the thinning algorithm to a stack of 2D planes. Figure 4c demonstrates that this method provides a preserved satisfactory thinned fracture network.

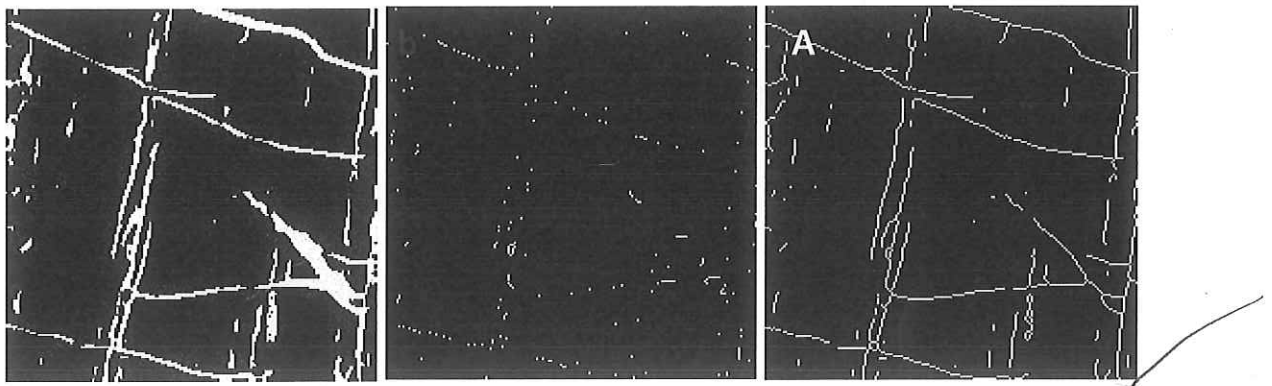


Figure 4. The thinned fracture construction. a: the entire fracture network, b: constructed thinned fracture using 3D thinning algorithm, c: constructed thinned fracture using stacks of skeleton the direction of flow.

5

Figure 4 displays the fracture aperture distribution of sample M2 before and after applying the calibration curve. This confirms that a significant amount of data is disregarded when non-calibrated images are used. This includes: (1) all of the fracture apertures with sizes smaller than the data resolution, and (2) fractures with aperture sizes larger than the resolution that are added to the connected flow network through new connection made by addition of the smaller fractures.

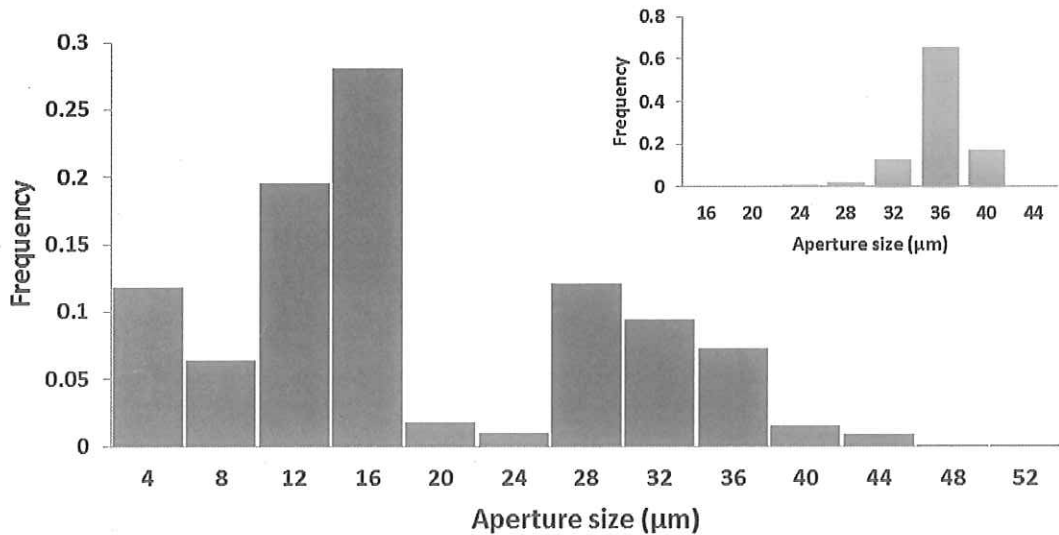


Figure 5. Fracture aperture distribution in the sample M2 after calibration and before calibration (the upper right graph).

To demonstrate the importance of image calibration for accurate flow simulation, the permeability of each image, M1 and M2, is initially measured in two different conditions: (1)

assuming entire resolved and sub-resolution fractures are fully permeable, (2) assuming only resolved fractures are permeable. The results are shown in Table 2, a large difference between two estimates is observed; however, none of the results are near to the experimental permeability of ~ 110 mD. Using only resolved fractures underestimates the permeability and including the sub-resolution and resolved fractures with no calibration overestimates the permeability. This indicates the significant error imposed by ignoring sub-resolution fractures (condition 1) or mislabeling the sub-resolution fractures (condition2).

Both images are then calibrated for fluid flow simulation. To calibrate the images, the subsets are upsampled by a factor of 4x, based on the results presented by [Ketcham et al. \(2010\)](#), to create images with a voxel size of ~ 4 μm . Then the segmented images are “thinned” and the corresponding aperture sizes are calculated using the equation derived from the calibration curve. Then the adjustment algorithm proceeds to open the weighted midpoint voxel aperture values to provide a 3D calibrated binary image for fluid flow simulation. Figure 6 shows the connected fractures for sample M2 before and after calibration. The permeability results for the calibrated images are shown in Table 2. The results of the calibrated images are reasonably in comparison to the experimental permeability. This occurs because the calibrated images include the resolved and sub-resolution fractures and adjusts aperture sizes. Therefore this preserves the original connectivity of the samples, which is critical for permeability measurements. To quantify the significance of including the entire network, the connectivity index and connectivity density of sample M1 and M2 are measured before and after calibration. The results presented in Table 2 show a clear increase in the connectivity of samples after applying the calibration technique that in turn has a direct influence on permeability. Overall, the calibration technique allows for capturing the correct topology and geometry of the fracture network that can be used for direct numerical simulations for the precise measurement of fractured rock permeability.

Table 2. The permeability and connectivity results for sample M1 and M2 before and after calibration.

Sample	Permeability mD				Experimental	Connectivity Index		Connectivity density (mm^{-1})	
	Condition 1	Condition 2	Calibrated			Before	After	Before	After
M1	3259	8.80E-03	90	110	274	144698	1.54	816.09	
M2	2627	5.85E-03	80		238	7391	11.24	349.08	

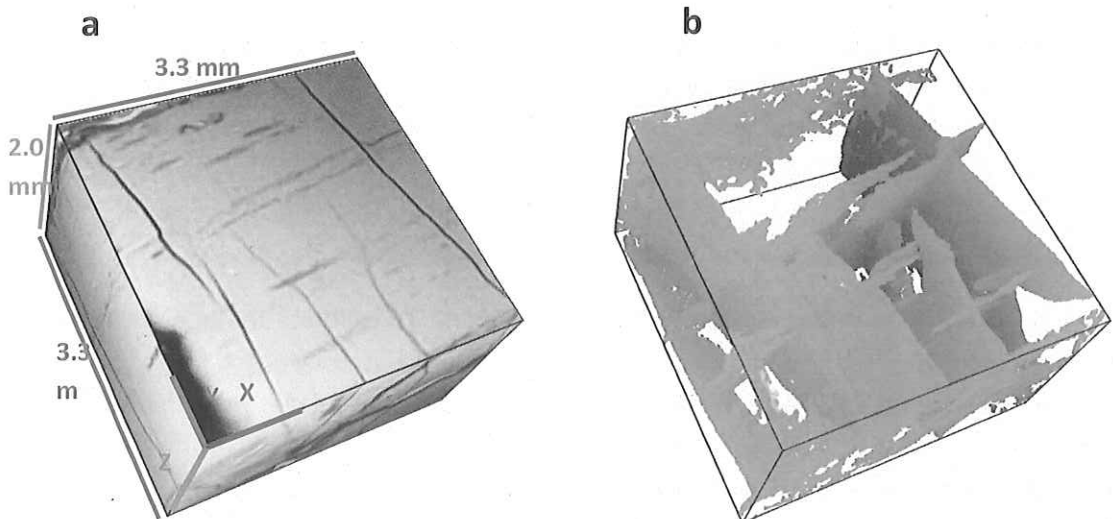


Figure 6. 3D visualization of sample M2. a: the difference image of the sample M2 (black= pores and fractures, gray= macerals and white = minerals), b: the connected fracture network of sample M2 before and after calibration (blue region is the only percolating region in the non-calibrated image while the entire network (blue and green) present in the connected network of calibrated image).

4. Conclusion and remarks

We obtained core-scale micro-CT images from a fractured rock sample in the air-filled and contrasting agent saturated conditions. Subtraction of these images reveals the features near the resolution limit of micro-CT. Subsequent segmentation of the resolved and sub-resolution fracture network using CAC and mathematical morphological techniques provides a complete fracture network. Two subsets are obtained from the sample for petrophysical analyses. The subsets are upsampled by 4x to enable assignment of aperture sizes smaller than the original data resolution. The gray-scale value at each fracture mid-point is extracted using a thinning algorithm applied to the segmented images. Then the gray-scale values are converted to the aperture sizes using the calibration curve. After that, the adjustment algorithm proceeds to grow the thinned fracture according to the calculated aperture values. This provides images in which the apertures are precisely assigned and original connectivities are preserved. The permeability of the images after and before calibration are computed and compared with the experimental permeability. Also the connectivity and aperture size distribution of the images after and before calibration are measured. The calibrated images result in permeability values near the experimental result. The connectivity and aperture size measurements indicate that the present calibration method preserves the true fracture geometry and topology and thus provides an accurate fracture network for flow simulations. Overall, the calibration technique allows for capturing the correct topology and geometry of the fracture network that can be

used for direct numerical simulations for the precise measurement of the fractured rock permeability.

5. References

- Armstrong, R.T., Georgiadis, A., Ott, H., Klemin, D., Berg, S., 2014a. Critical capillary number: Desaturation studied with fast X-ray computed microtomography. *Geophysical Research Letters* 41, 55-60.
- Armstrong, R.T., Ott, H., Georgiadis, A., Rücker, M., Schwing, A., Berg, S., 2014b. Subsecond pore-scale displacement processes and relaxation dynamics in multiphase flow. *Water resources research* 50, 9162-9176.
- Arns, C., Bauget, F., Sakellariou, A., Senden, T., Sheppard, A., Sok, R., Ghous, A., Pinczewski, W., Knackstedt, M., Kelly, J., 2005. Digital core laboratory: Petrophysical analysis from 3D imaging of reservoir core fragments. *Petrophysics* 46.
- Berg, S., Armstrong, R., Ott, H., Georgiadis, A., Klapp, S., Schwing, A., Neiteler, R., Brussee, N., Makurat, A., Leu, L., 2014. Multiphase flow in porous rock imaged under dynamic flow conditions with fast X-ray computed microtomography. *Petrophysics* 55, 304-312.
- Brown, S.R., Kranz, R.L., Bonner, B.P., 1986. Correlation between the surfaces of natural rock joints. *Geophysical Research Letters* 13, 1430-1433.
- Buie, H.R., Campbell, G.M., Klinck, R.J., MacNeil, J.A., Boyd, S.K., 2007. Automatic segmentation of cortical and trabecular compartments based on a dual threshold technique for in vivo micro-CT bone analysis. *Bone* 41, 505-515.
- Cantrell, B., Michaels, W., 2010. Digital drawing for landscape architecture: contemporary techniques and tools for digital representation in site design. John Wiley & Sons.
- Caselles, V., Kimmel, R., Sapiro, G., 1997. Geodesic active contours. *International journal of computer vision* 22, 61-79.
- Catmull, E., Rom, R., 1974. A class of local interpolating splines. *Computer aided geometric design* 74, 317-326.
- Clarkson, C.R., Marc Bustin, R., 1996. Variation in micropore capacity and size distribution with composition in bituminous coal of the Western Canadian Sedimentary Basin: Implications for coalbed methane potential. *Fuel* 75, 1483-1498.
- Close, J.C., Mavor, M.J., 1991. Influence of Coal Composition and Rank on Fracture Development in Fruitland Coal Gas Reservoirs of San Juan Basin. Coalbed methane of western North America, Rocky Mountain Association of Geologists, 109–121.
- Detwiler, R.L., Pringle, S.E., Glass, R.J., 1999. Measurement of fracture aperture fields using transmitted light: An evaluation of measurement errors and their influence on simulations of flow and transport through a single fracture. *Water Resources Research* 35, 2605-2617.
- Dong, P., 1997. Implementation of mathematical morphological operations for spatial data processing. *Computers & Geosciences* 23, 103-107.
- Gamson, P.D., Beamish, B.B., Johnson, D.P., 1993. Coal microstructure and micropermeability and their effects on natural gas recovery. *Fuel* 72, 87-99.
- Gangi, A.F., 1978. Variation of whole and fractured porous rock permeability with confining pressure, *International Journal of Rock Mechanics and Mining Sciences & Geomechanics Abstracts*. Elsevier, pp. 249-257.
- Gentier, S., Billiaux, D., Vliet, L., 1989. Laboratory testing of the voids of a fracture. *Rock Mech Rock Engng* 22, 149-157.

- Huo, D., Pini, R., Benson, S.M., 2016. A calibration-free approach for measuring fracture aperture distributions using X-ray computed tomography. *Geosphere*, GES01175. 01171.
- Illman, W.A., 2006. Strong field evidence of directional permeability scale effect in fractured rock. *Journal of Hydrology* 319, 227-236.
- James, J., 2012. Digital intermediates for film and video. Focal Press, UK.
- Jazayeri Noushabadi, M.R., Jourde, H., Massonnat, G., 2011. Influence of the observation scale on permeability estimation at local and regional scales through well tests in a fractured and karstic aquifer (Lez aquifer, Southern France). *Journal of Hydrology* 403, 321-336.
- Johns, R.A., Steude, J.S., Castanier, L.M., Roberts, P.V., 1993. Nondestructive measurements of fracture aperture in crystalline rock cores using X ray computed tomography. *Journal of Geophysical Research: Solid Earth* 98, 1889-1900.
- Jones, A.C., Arns, C.H., Sheppard, A.P., Hutmacher, D.W., Milthorpe, B.K., Knackstedt, M.A., 2007. Assessment of bone ingrowth into porous biomaterials using MICRO-CT. *Biomaterials* 28, 2491-2504.
- Jones, S.C., 1972. A rapid accurate unsteady-state Klinkenberg permeameter. *Society of Petroleum Engineers Journal* 12, 383-397.
- Keller, A., 1998. High resolution, non-destructive measurement and characterization of fracture apertures. *International Journal of Rock Mechanics and Mining Sciences* 35, 1037-1050.
- Ketcham, R.A., 2005. Computational methods for quantitative analysis of three-dimensional features in geological specimens. *Geosphere* 1, 32-41.
- Ketcham, R.A., Carlson, W.D., 2001. Acquisition, optimization and interpretation of X-ray computed tomographic imagery: applications to the geosciences. *Computers & Geosciences* 27, 381-400.
- Ketcham, R.A., Slottke, D.T., Sharp, J.M., 2010. Three-dimensional measurement of fractures in heterogeneous materials using high-resolution X-ray computed tomography. *Geosphere* 6, 499-514.
- Knackstedt, M.A., Arns, C.H., Sok, R.M., Sheppard, A.P., 2007. 3D Pore Scale Characterisation of Carbonate Core: Relating pore types and interconnectivity to petrophysical and multiphase flow properties, International Petroleum Technology Conference. International Petroleum Technology Conference.
- Kumar, A.T., Majors, P.D., Rossen, W., 1997. Measurement of Aperture and Multiphase Flow in Fractures using NMR Imaging. *SPE Formation Evaluation* 12, 101-108.
- Latham, J.-P., Xiang, J., Belayneh, M., Nick, H.M., Tsang, C.-F., Blunt, M.J., 2013. Modelling stress-dependent permeability in fractured rock including effects of propagating and bending fractures. *International Journal of Rock Mechanics and Mining Sciences* 57, 100-112.
- Latham, S., Varslot, T., Sheppard, A., 2008. Image registration: enhancing and calibrating X-ray micro-CT imaging. Proc. of the Soc. Core Analysts, Abu Dhabi, UAE.
- Laubach, S., Tremain, C., 1991. Regional coal fracture patterns and coalbed methane development, The 32nd US Symposium on Rock Mechanics (USRMS), Norman, Oklahoma.
- Laubach, S.E., Marrett, R.A., Olson, I.E., Scott, A.R., 1998. Characteristics and origins of coal cleat: a review. *International Journal of Coal Geology* 35, 175-207.
- Lee, T.C., Kashyap, R.L., Chu, C.N., 1994. Building Skeleton Models via 3-D Medial Surface Axis Thinning Algorithms. *CVGIP: Graphical Models and Image Processing* 56, 462-478.
- Leone, P., Chow, W.-C., Gill, A., 2009. Chroma upsampling method and apparatus therefor. Google Patents.
- Lindquist, W.B., Lee, S.M., Coker, D.A., Jones, K.W., Spanne, P., 1996. Medial axis analysis of void structure in three-dimensional tomographic images of porous media. *Journal of Geophysical Research: Solid Earth* (1978–2012) 101, 8297-8310.
- Lindquist, W.B., Venkatarangan, A., 1999. Investigating 3D geometry of porous media from high resolution images. *Physics and Chemistry of the Earth, Part A: Solid Earth and Geodesy* 24, 593-599.

- Mazumder, S., Wolf, K.H.A.A., Elewaut, K., Ephraim, R., 2006. Application of X-ray computed tomography for analyzing cleat spacing and cleat aperture in coal samples. International Journal of Coal Geology 68, 205-222.
- Moore, T.A., 2012. Coalbed methane: A review. International Journal of Coal Geology 101, 36-81.
- Mostaghimi, P., Armstrong, R.T., Gerami, A., Ebrahimi Warkaini, M., Lamei Ramandi, H., Pinczewski, V., 2015. Micro-CT imaging and microfluidics for understanding flow in coal seam reservoirs, International Symposium of the Society of Core Analysts, Newfoundland, Canada.
- Mostaghimi, P., Mahani, H., 2010. A quantitative and qualitative comparison of coarse-grid-generation techniques for modeling fluid displacement in heterogeneous porous media. SPE Reservoir Evaluation & Engineering 13, 24-36.
- Mostaghimi, P., Tollit, B.S., Neethling, S.J., Gorman, G.J., Pain, C.C., 2014. A control volume finite element method for adaptive mesh simulation of flow in heap leaching. Journal of Engineering Mathematics 87, 111-121.
- Odgaard, A., Gundersen, H., 1993. Quantification of connectivity in cancellous bone, with special emphasis on 3-D reconstructions. Bone 14, 173-182.
- Ortega, O.J., Marrett, R.A., Laubach, S.E., 2006. A scale-independent approach to fracture intensity and average spacing measurement. AAPG bulletin 90, 193-208.
- Peyton, R.L., Haefner, B.A., Anderson, S.H., Gantzer, C.J., 1992. Applying X-ray CT to measure macropore diameters in undisturbed soil cores. Geoderma 53, 329-340.
- Pudney, C., 1998. Distance-Ordered Homotopic Thinning: A Skeletonization Algorithm for 3D Digital Images. Computer Vision and Image Understanding 72, 404-413.
- Puri, R., Evanoff, J., Brugler, M., 1991. Measurement of coal cleat porosity and relative permeability characteristics, SPE Gas Technology Symposium. Society of Petroleum Engineers, Houston, Texas.
- Pyrack-Nolte, L.J., Myer, L.R., Cook, N.G.W., Witherspoon, P.A., 1987. Hydraulic and mechanical properties of natural fractures in low-permeability rock.
- Quackenbush, L.J., 2004. A review of techniques for extracting linear features from imagery. Photogrammetric Engineering & Remote Sensing 70, 1383-1392.
- Ramandi, H.L., Armstrong, R.T., Mostaghimi, P., 2016a. Micro-CT image calibration to improve fracture aperture measurement. Case Studies in Nondestructive Testing and Evaluation.
- Ramandi, H.L., Armstrong, R.T., Mostaghimi, P., Saadatfar, M., Pinczewski, W.V., 2015. X-Ray Micro-Computed Tomography Imaging for Coal Characterization, SPE Asia Pacific Unconventional Resources Conference and Exhibition. Society of Petroleum Engineers, Brisbane.
- Ramandi, H.L., Mostaghimi, P., Armstrong, R.T., Saadatfar, M., Pinczewski, W.V., 2016b. Porosity and permeability characterization of coal: a micro-computed tomography study. International Journal of Coal Geology 154–155, 57-68.
- Renshaw, C.E., Dadakis, J.S., Brown, S.R., 2000. Measuring fracture apertures: A comparison of methods. Geophysical Research Letters 27, 289-292.
- Robert, A.J., John, S.S., Louis, M.C., Paul, V.R., 1993. Nondestructive measurements of fracture aperture in crystalline rock cores using X ray computed tomography. Journal of Geophysical Research: Solid Earth (1978–2012) 98, 1889-1900.
- Saadatfar, M., Francois, N., Arad, A., Madadi, M., Cruikshank, R., Alizadeh, M., Sheppard, A., Kingston, A., Limay, A., Senden, T., Knackstedt, M., 3D mapping of deformation in an unconsolidated sand: A micro mechanical study, SEG Technical Program Expanded Abstracts 2012, pp. 1-6.
- Sakellariou, A., Arns, C.H., Sheppard, A.P., Sok, R.M., Averdunk, H., Limaye, A., Jones, A.C., Senden, T.J., Knackstedt, M.A., 2007. Developing a virtual materials laboratory. Materials Today 10, 44-51.
- Scheidegger, A.E., 1963. Physics of flow through porous media, Physics of flow through porous media. University of Toronto.

- Schlüter, S., Sheppard, A., Brown, K., Wildenschild, D., 2014. Image processing of multiphase images obtained via X-ray microtomography: A review. *Water Resources Research* 50, 3615-3639.
- Serra, J., 1986. Introduction to mathematical morphology. *Computer vision, graphics, and image processing* 35, 283-305.
- Sheppard, A., Latham, S., Middleton, J., Kingston, A., Myers, G., Varslot, T., Fogden, A., Sawkins, T., Cruikshank, R., Saadatfar, M., Francois, N., Arns, C., Senden, T., 2014. Techniques in helical scanning, dynamic imaging and image segmentation for improved quantitative analysis with X-ray micro-CT. *Nuclear Instruments and Methods in Physics Research Section B: Beam Interactions with Materials and Atoms* 324, 49-56.
- Sheppard, A.P., Sok, R.M., Averdunk, H., 2004. Techniques for image enhancement and segmentation of tomographic images of porous materials. *Physica A: Statistical Mechanics and its Applications* 339, 145-151.
- Sok, R.M., Varslot, T., Ghous, A., Latham, S., Sheppard, A.P., Knackstedt, M.A., 2010. Pore scale characterization of carbonates at multiple scales: Integration of micro-CT, BSEM, FIBSEM. *Petrophysics* 51, 379.
- Su, X., Feng, Y., Chen, J., Pan, J., 2001. The characteristics and origins of cleat in coal from Western North China. *International Journal of Coal Geology* 47, 51-62.
- Ting, F.T.C., 1977. ORIGIN AND SPACING OF CLEATS IN COAL BEDS. *Journal of Pressure Vessel Technology, Transactions of the ASME* 99 Ser J, 624-626.
- Van Geet, M., Swennen, R., 2001. Quantitative 3D-fracture analysis by means of microfocus X-Ray Computer Tomography (μ CT): An example from coal. *Geophysical Research Letters* 28, 3333-3336.
- Vandersteen, K., Busselen, B., Van Den Abeele, K., Carmeliet, J., 2003. Quantitative characterization of fracture apertures using microfocus computed tomography. *Geological Society, London, Special Publications* 215, 61-68.
- Verhelst, F., Vervoort, A., BOSSCHER, P.D., Marchal, G., 1995. X-ray computerized tomography: determination of heterogeneities in rock samples, 8th ISRM Congress.
- Vincent, L., Soille, P., 1991. Watersheds in Digital Spaces - an Efficient Algorithm Based on Immersion Simulations. *Ieee T Pattern Anal* 13, 583-598.
- Wang, J.A., Park, H.D., 2002. Fluid permeability of sedimentary rocks in a complete stress-strain process. *Engineering Geology* 63, 291-300.
- Weerakone, W.M.S.B., Wong, R.C.K., 2010. Characterization of Variable Aperture Rock Fractures Using X-ray Computer Tomography, *Advances in X-ray Tomography for Geomaterials*. ISTE, pp. 229-235.
- Yao, Y., Liu, D., Che, Y., Tang, D., Tang, S., Huang, W., 2009. Non-destructive characterization of coal samples from China using microfocus X-ray computed tomography. *International Journal of Coal Geology* 80, 113-123.

***Highlights (3 to 5 bullet points (maximum 85 characters including spaces per bullet point)**

- A novel method is developed for prediction of fractured rock permeability using micro-CT imaging.
- The skeleton of the fracture system is extracted based on micro-CT images while the aperture is obtained using SEM data.
- The computed permeability is compared with experimental measurements.
- Connectivity of the fractured system is analyzed based on micro-CT and SEM data.

